Supporting Information

Disclosing Multiple Factors Influencing Enantioselective CO_2 and *Meso*-Epoxides Copolymerization with β-Diiminate Zn Catalysts

Yolanda Rusconi,[a,b] Massimo Christian D'Alterio,[b] Claudio De Rosa,[b] Geoffrey W. Coates,[c] Giovanni Talarico*[a,b]

[a]Scuola Superiore Meridionale, Largo San Marcellino, 80138, Napoli, Italy

[b]Dipartimento di Scienze Chimiche, Università degli Studi di Napoli Federico II, 80126, Napoli, Italy.

[c]Department of Chemistry and Chemical Biology, Baker Laboratory, Cornell University, Ithaca, NY 14853-1301, USA

Corresponding: talarico@unina.it

Table of contents

1. Additional computational details

The Gibbs energies calculated for the carbon dioxide insertion (TS2) are corrected for the translational entropy contributions following the Martin procedure[1] modified by us[2] for the ROP of CHO/CO_2. In addition to the standard computational method reported in the main text, we employed also the computational approach used by Cramer[3] and the optimized geometries using the B3LYP-D3BJ[4,5] functional, with LANL2DZ[6] for Zn and 6-31G(d) for all the other atoms were refined with single-point (SP) energies using ωB97XD,[7] with SDD[8] for Zn and 6-311+G(d,p) for all other atoms. Solvation was considered in the SP calculation using the SMD[9] model in toluene. The calculated enantioselectivity for **BD1-D*syn*** species using three different computational protocols are reported in Table S1.

Table S1 DFT enantioselectivities (Gibbs energies, kcal/mol) for the propagation promoted by **BDI1-D*syn*** at different levels of theory for geometry optimization and single-point calculations.

<table>
<tr><th colspan="5">Propagation BDI1-D<i>syn</i>
Enantioselectivity $\Delta\Delta G_{\text{enantio}}$ (kcal·mol^{-1})</th></tr>
<tr><td rowspan="3">Optimization</td><td>B3LYP/SVP/SDD</td><td>2.9</td><td>B3LYP-D3BJ(PCM)/SDD/
6-311G(d,p)</td><td rowspan="3">Single-point</td></tr>
<tr><td>B3LYP/SVP/SDD</td><td>2.9</td><td>ωB97XD(SMD)/SDD/
6-311G+(d,p)</td></tr>
<tr><td>B3LYP-D3BJ/LANL2DZ/
6-31G(d)</td><td>2.1</td><td>ωB97XD(SMD)/SDD/
6-311G+(d,p)</td></tr>
</table>

The conformations of the growing chains were optimized through a conformational study. The analysis was performed on a model of (*S*)-PCHC, a *trans*-(*S,S*)-(2-methoxycarbonyloxycyclohexyl) methyl carbonate, as reported in Scheme S1. Conformational energy calculations were carried out using computational methods on the model of Scheme S1 which is defined by five torsion angles: θ_1, θ_2, θ_2', θ_3, and θ_3'. The dihedral angle θ_1 was fixed at approximately 60° (G^+) in this analysis due to the chemical structure, as it is determined by the four O-(*S*)CH-(*S*)CH-O atoms, with (*S*)C and (*S*)C attached to the cyclohexyl ring. Deviations from this value lead to significant distortions in the O-C-H bond angles, departing from the ideal 109° geometry. For the dihedral angles θ_3 and θ_3', an initial value of 180° (T) was assumed, as it is a common minimum for dihedral angles involving ester and carbonate bonds. The conformational energy of (*S*)-PCHC was then calculated as a function of the torsion angles θ_2 and θ_2', with θ_1, θ_3, and θ_3' allowed to optimize freely. The results of this analysis reveal a shallow energy minimum zone. The global minimum occurs at $\theta_2 = -150°$ (A^-) and $\theta_2' = -150°$ (A^-). This result is mirrored for the (*R*)-PCHC chain, where the global minimum occurs at $\theta_2 = +150°$ (A^+) and $\theta_2' = +150°$ (A^+). Following identification of the minima for (*S*) and (*R*) growing chains, we located the transition state and intermediate structures. It is important to note that although the initial guess was based on the global minimum, the dihedral angles underwent slight changes during the optimization although remaining in the shallow minimum zone. Finally, as expected, the freely optimized θ_3 and θ_3' values remained close to 180° (T) without significant deviations.

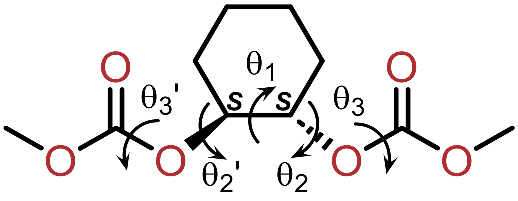

Scheme S1 Portion of the chain of (*S*)-PCHC and definition of the torsion angles θ_1, θ_2, θ_2' θ_3, θ_3'. Hydrogen atoms are not shown.

1.1 Details of ASM analysis

The activation strain model analysis[10,11] has been performed separating the transition states of interest into two fragments. The catalyst precursor + growing chain has been chosen as Fragment 1 (the example of **BDI1-D*anti*** is reported in Fig. S2, left), the monomer as Fragment 2 (Fig. S2, right). Single-point calculations of each fragment have been performed using the methods explained in the main text, without solvent. Subtraction of the energetic values obtained from these calculations have been subtracted by the energy calculated for reference structures.

$\Delta E_{\text{Strain (Frag,1)}} = \Delta E_{\text{ (Frag,1)}} - \Delta E_{\text{(Reference)}}$

$\Delta E_{\text{Strain (Frag,2)}} = \Delta E_{\text{(Frag,2)}} - \Delta E_{\text{(Reference)}}$

ΔE_{Strain} has then been calculated as the sum of the ΔE_{Strain} values of each fragment:

$\Delta E_{\text{Strain}} = \Delta E_{\text{Strain (Frag,1)}} + \Delta E_{\text{Strain (Frag,2)}}$

1.2 Details of %V_{Bur} analysis

The %V_{Bur} of the octants (1/8 of a sphere, see Fig. S3) in each TS reported in the main text have been calculated by using a sphere radius of 5.0 Å and mesh size of 0.10. The acetate and CHO atoms were deleted from the TSs. H and Zn atoms were not included in the calculation. For **BDI-M** species we used: Zn atom as center of the sphere; C_2 of the ligand backbone as negative z; C_4 of 2,6-dimethylphenyl substituent for xz-plane definition. For **BDI1-D** we added two dummy atoms in the following positions: dummy atom 1 in the middle of the Zn-Zn bond; dummy atom 2 forming a 90° angle with Zn and dummy atom 1. The %V_{Bur} were calculated by using the SambVca 2.1 tool,[12] choosing: dummy atom 1 as center of the sphere; dummy atom 2 as positive z; Zn atom for xz-plane definition.

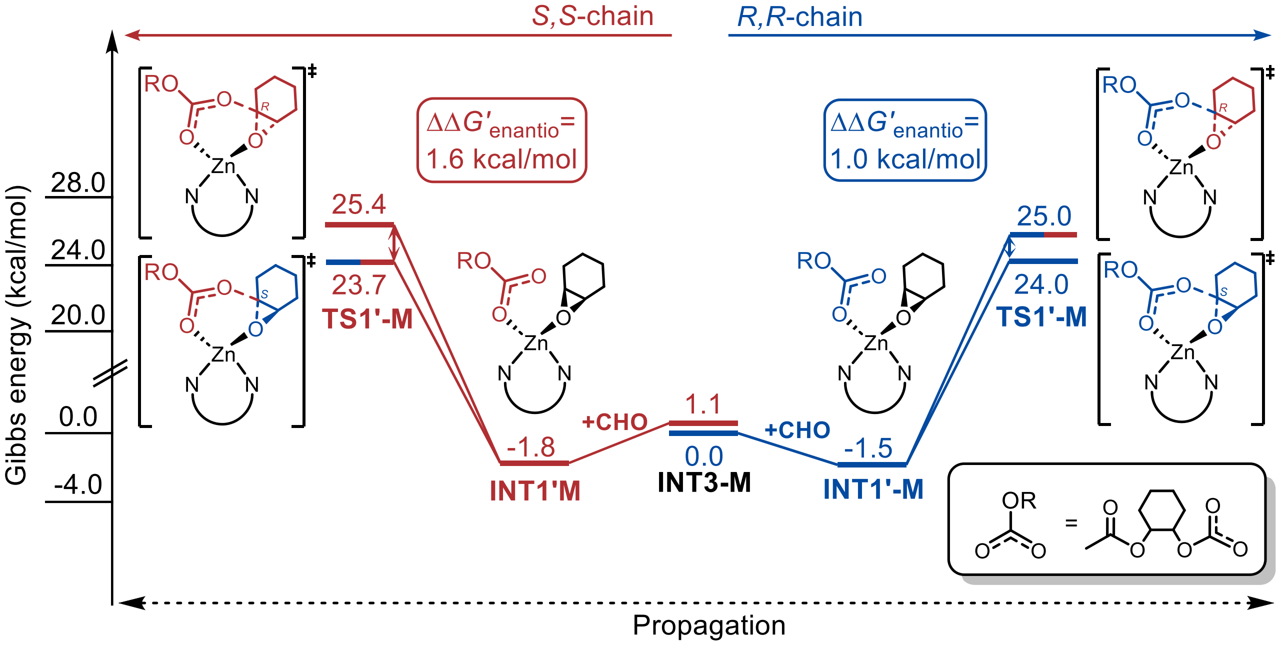

Fig. S1 Gibbs energies (kcal/mol) for the minimum energy path of CHO ring-opening promoted by **BDI1-M** by using the *R,R*- (right) and *S,S*-configured growing unit (left). Gibbs energies calculated with respect to the INT3-$M_{R,R}$ species. The presence of an entire growing unit ($(OR)CO_2^-$) is simulated.

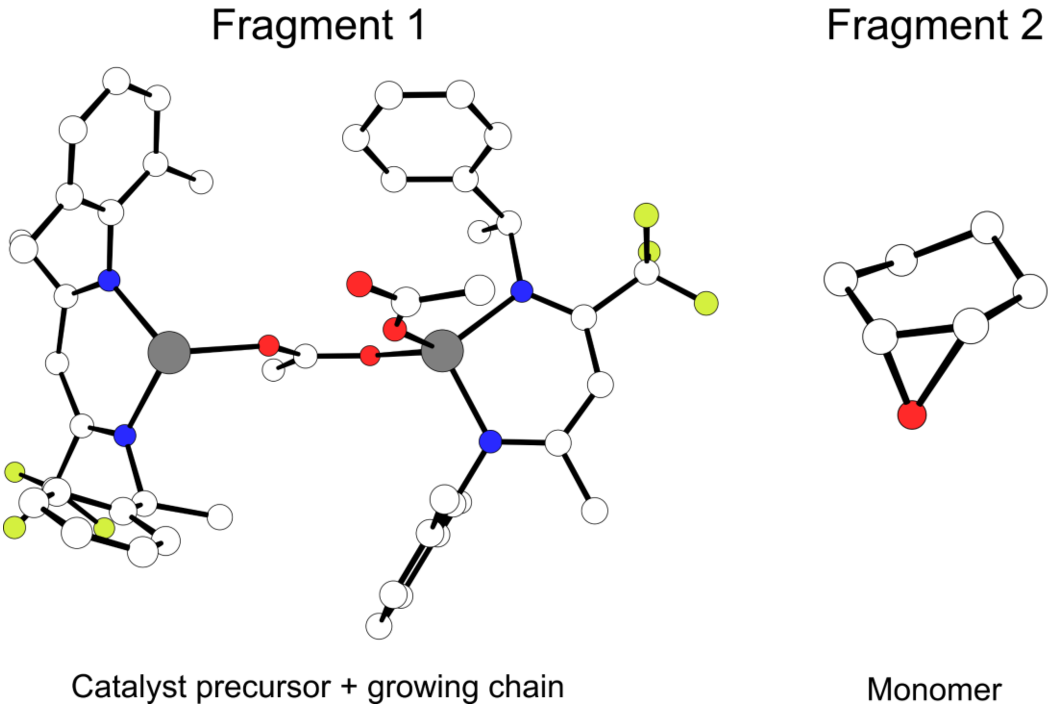

Fig. S2 Example of the fragments chosen for the ASM analysis. Fragment 1: Catalyst precursor + growing chain (left), fragment 2: monomer (right).

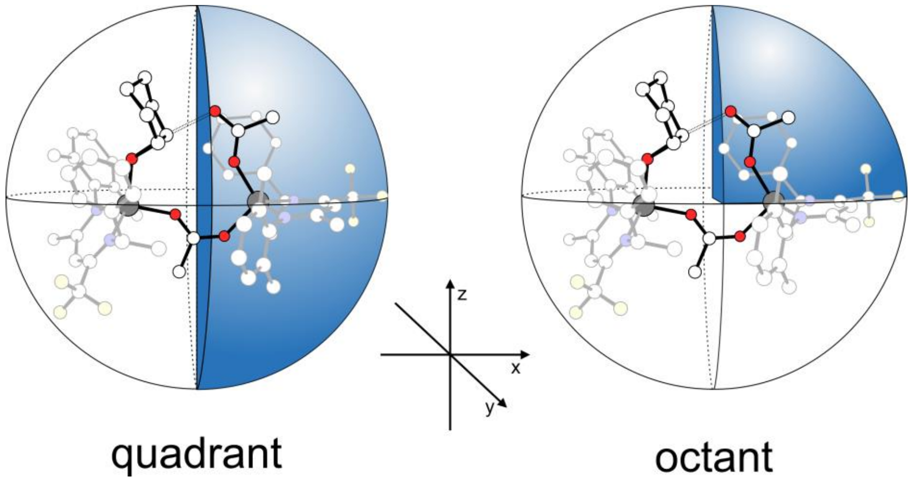

Fig. S3 Illustrative 3D representation of quadrants (left) and octants (right) in the calculated sphere for the %V_{Bur} analysis.

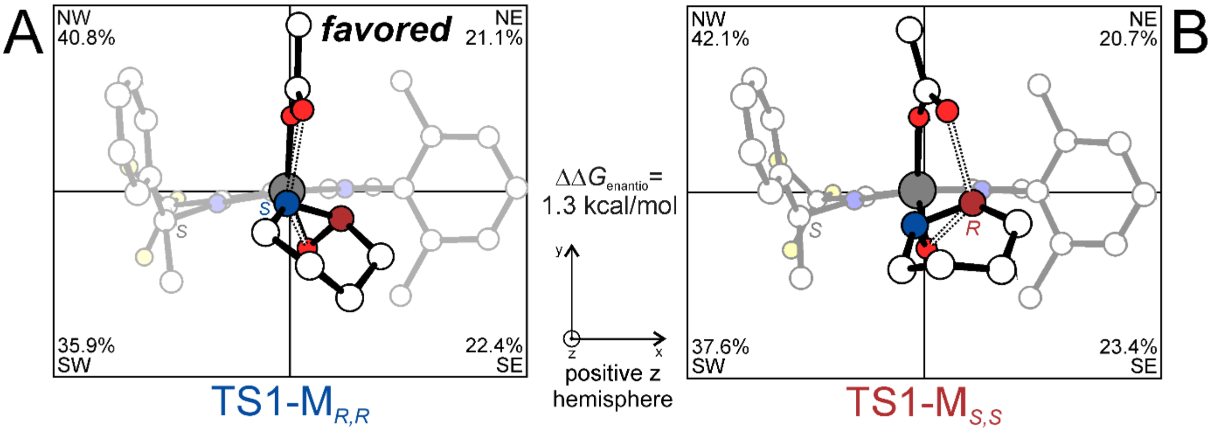

Fig. S4 DFT optimized geometries for TS1-M with the attack to *S* (A) and *R* (B) CHO stereocenters with the steric maps calculated by %V_{Bur} for the initiation steps promoted by **BDI1-M**.

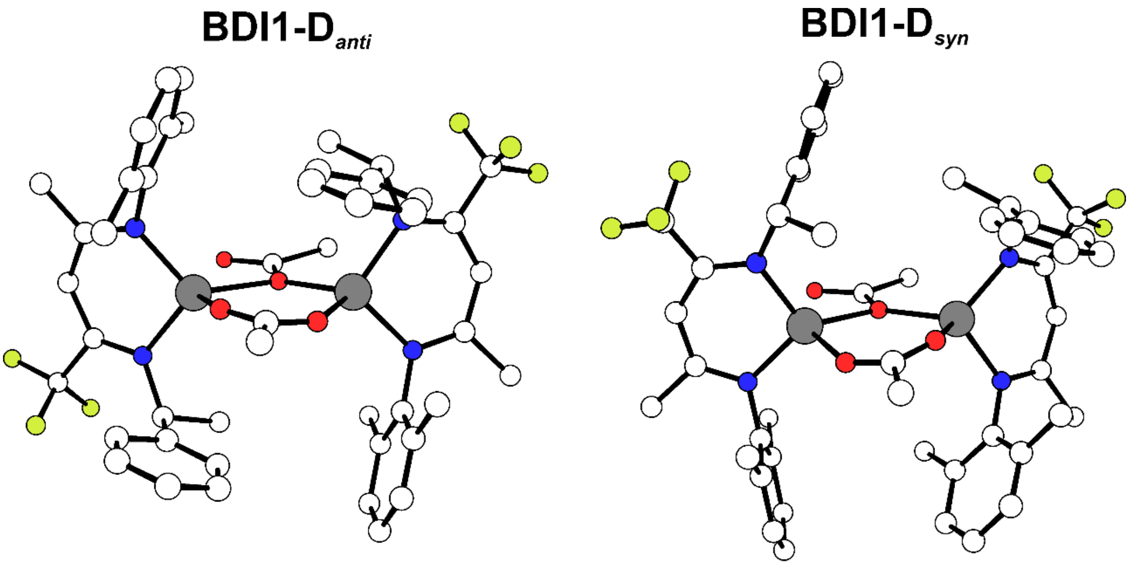

BDI1-D$_{anti}$ **BDI1-D$_{syn}$**

ΔG_{dim} = -11.0 kcal/mol ΔG_{dim} = -5.9 kcal/mol

$\Delta\Delta G$ = 4.9 kcal/mol

Fig. S5 Optimized structures **BDI1-D*anti*** (left) and **BDI1-D*syn*** (right) precursors.

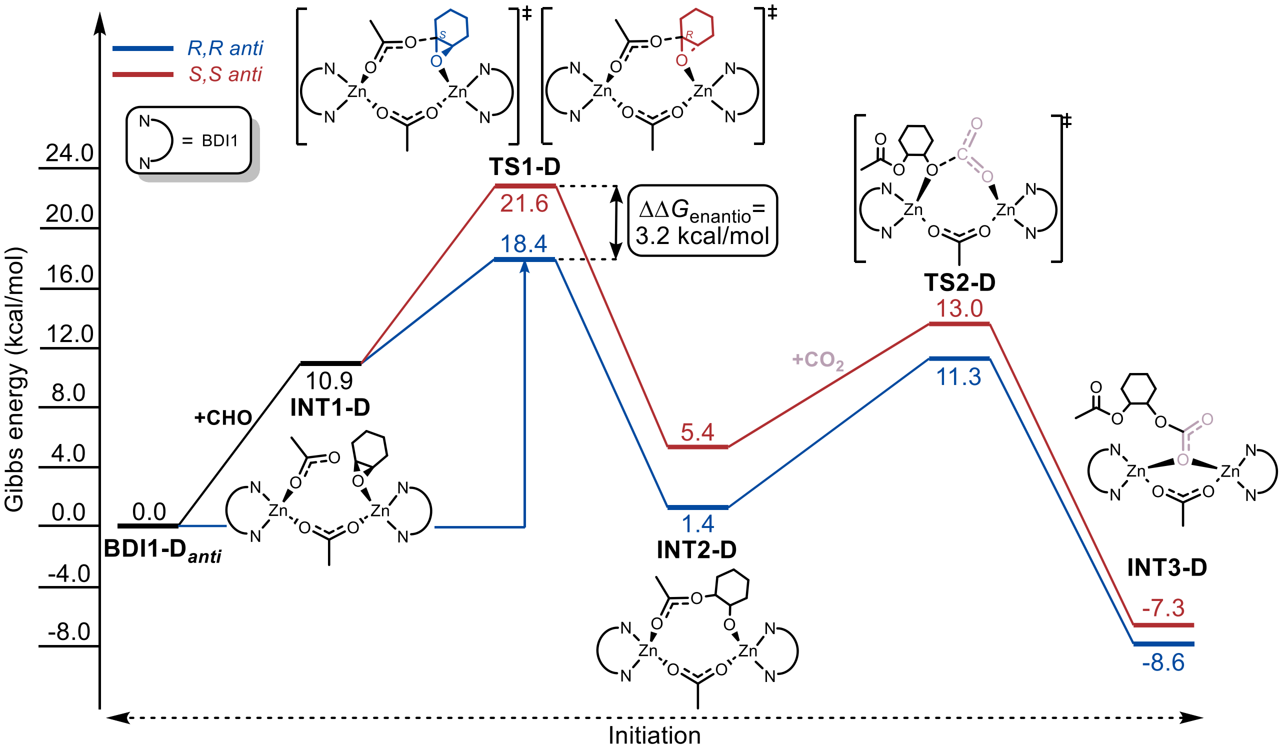

Fig. S6 Gibbs energetic profile (kcal/mol) of the initiation reaction for the copolymerization of CHO and CO_2 at **BDI1-D$_{anti}$**. Gibbs energies calculated with respect to the more stable **BDI1-D$_{anti}$** species. The paths leading to the formation of *R,R*-chain and *S,S*-chain are reported respectively in blue and red.

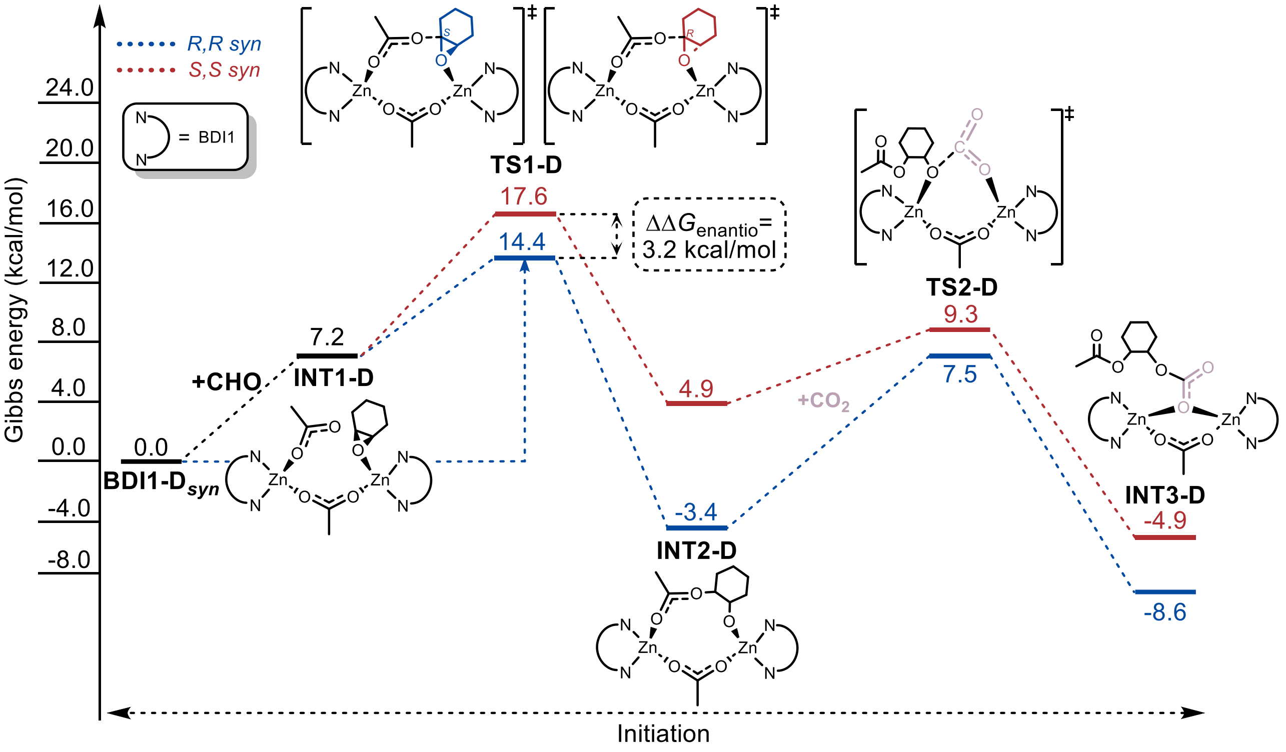

Fig. S7 Gibbs energetic profile (kcal/mol) of the initiation reaction for the copolymerization of CHO and CO_2 at **BDI1-D*syn***. Gibbs energies calculated with respect to the more stable **BDI1-D*syn*** species. The paths leading to the formation of *R,R*-chain and *S,S*-chain are reported respectively in blue and red.

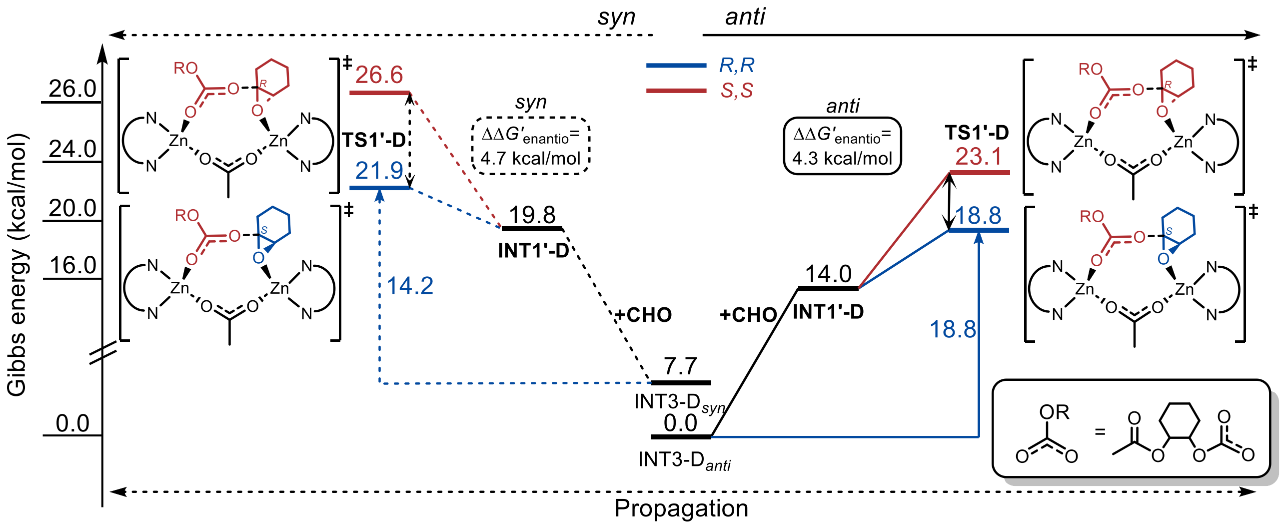

Fig. S8 Minimum energy path for the CHO ring-opening on a *S,S*-configured growing unit, by **BDI1-D$_{syn}$** (left) and **BDI1-D$_{anti}$** (right). Gibbs energies (kcal/mol) calculated with respect to the more stable INT3-D$_{anti\text{-}R,R}$ species. The paths leading to *R,R*- and *S,S*-chain formation are reported respectively in blue and red.

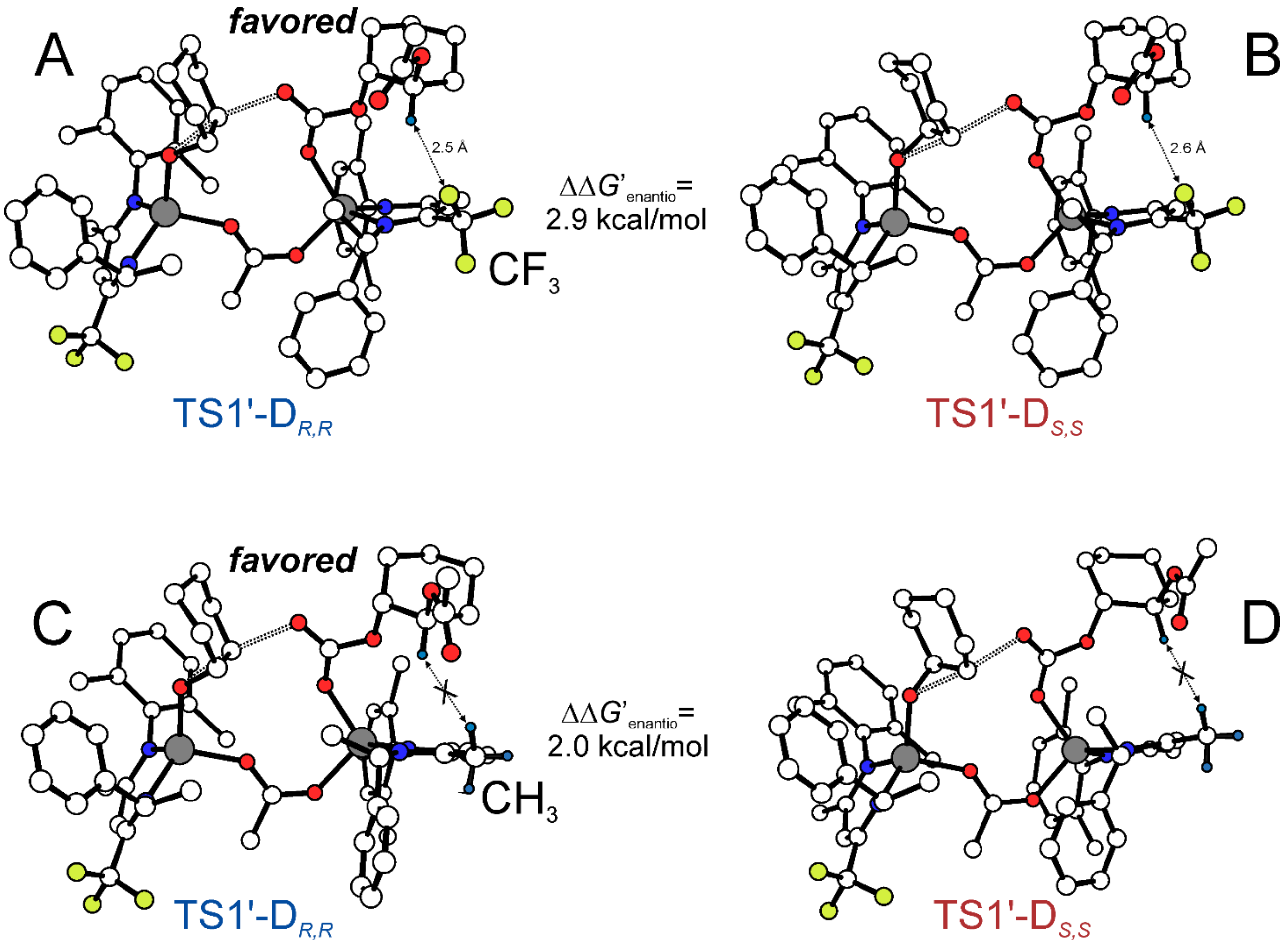

Fig. S9 Optimized structures of the RDS of **BDI1-D*syn*** species for the propagation of the ROCOP of CO_2 and epoxides, with unmodified system (A and B) and after replacement of $-CF_3$ with $-CH_3$ (C and D). The presence of NCI between a hydrogen of the growing chain and F atom of the catalyst is indicated by arrows.

Table S2 ASM results for selected TSs leading to the enantioselectivity of the initiation (TS1) and propagation (TS1’) steps for ROCOP of CO_2 and CHO promoted by **BDI5-D*syn***.

	Initiation			Propagation		
	TS1-D$_{R,R}$	TS1-D$_{S,S}$	$\Delta\Delta E$	TS1’-D$_{R,R}$	TS1’-D$_{S,S}$	$\Delta\Delta E$
$\Delta E_{\mathrm{Strain}}$	73.6	75.4	1.9	73.6	76.9	3.3
$\Delta E_{\mathrm{Strain(Cat+chain)}}$	47.6	47.4	-0.2	46.8	48.7	**1.9**
$\Delta E_{\mathrm{Strain(Mon)}}$	21.9	23.9	**1.7**	26.9	28.3	**1.4**

References

1. R. L. Martin, P. J. Hay, and L. R. Pratt, *J. Phys. Chem. A*, 1998, **102**, 3565-3573.
2. L. Falivene, V. Barone, and G. Talarico, *Mol. Catal.*, 2018, **452**, 138-144.
3. H. Shao, Y. Reddi, and C. J. Cramer, *ACS Catal.*, 2020, **10**, 8870-8879.
4. C. Lee, W. Yang, and R. G. Parr, *Phys. Rev. B*, 1988, **37**, 785-789.
5. A. D. Becke, *J. Chem. Phys.*, 1993, **98**, 5648-5652.
6. S. Grimme, *J. Comput. Chem.*, 2006, **27**, 1787-1799.
7. J.-D. Chai and M. Head-Gordon, *Phys. Chem. Chem. Phys.*, 2008, **10**, 6615-6620.
8. F. Weigend and R. Ahlrichs, *Phys. Chem. Chem. Phys.*, 2005, **7**, 3297-3305.
9. A. V. Marenich, C. J. Cramer, and D. G. Truhlar, *J. Phys. Chem. B*, 2009, **113**, 6378-6396.
10. P. Vermeeren, S. C. C. van der Lubbe, C. Fonseca Guerra, F. M. Bickelhaupt, and T. A. Hamlin, *Nat. Prot.*, 2020, **15**, 649-667.
11. F. M. Bickelhaupt and K. N. Houk, *Angew. Chem., Int. Ed.*, 2017, **56**, 10070-10086.
12. L. Falivene, Z. Cao, A. Petta, L. Serra, A. Poater, R. Oliva, V. Scarano, and L. Cavallo, *Nat. Chem.*, 2019, **11**, 872-879.